



Anterior and posterior imaging with hyperparallel OCT

STEVE FRISKEN, TREVOR ANDERSON,* ARMIN SEGREF, DIRK LORENSER, AND GRANT FRISKEN

Cylite Ltd. Pty., Victoria 3070, Australia

*trevor.anderson@cyliteoptics.com

Abstract: Hyperparallel OCT (HP-OCT) is a parallel spectral domain imaging technology particularly well-suited to the anterior segment. It uses a 2-dimensional grid of 1008 beams to simultaneously image across a wide area of the eye. In this paper we demonstrate that sparsely sampled volumes captured at 300 Hz can be registered without the need for active eye tracking to produce 3-dimensional (3D) volumes free from motion artefacts. The anterior volume provides complete 3D biometric information, including lens position, curvature, epithelial thickness, tilt, and axial length. We further demonstrate that, with the change of a detachable lens, we can capture high resolution anterior volumes and importantly, posterior volume images for preoperative assessment of the posterior segment. Advantageously, the retinal volumes have the same 11.2 mm Nyquist range as the anterior imaging mode.

© 2023 Optica Publishing Group under the terms of the [Optica Open Access Publishing Agreement](#)

1. Introduction

Anterior segment (AS) biometry dictates an optimal imaging width and depth much larger than typical posterior segment OCT systems which have an imaging depth an order of magnitude less than that required to image the entire anterior chamber and lens [1–4]. Whilst lens adaptors to image the anterior segment have been developed for many posterior segment (PS) OCT systems, they are, however, ill-adapted to the more general requirements of accurate, quantitative biometry and surface curvature measurement. This is due to three major limitations: firstly, the typical depth range of posterior OCT is insufficient to image the whole anterior chamber; secondly, the difficulty of absolute calibration of the scanning-induced distortions in location and trajectory of each acquired A-scan; and thirdly, patient motion while scanning causes artefacts or errors. Eye-tracking and registration techniques [5] have been developed for posterior segment OCT [6], based on the many available registration features (capillary structure, optic nerve, etc). However AS lacks the high contrast features in the cornea that would allow tracking of the ocular position and orientation with the degree of accuracy required to enable the resultant volumes to be used for metrology.

The registration challenge for conventional OCT approaches to AS biometry is highlighted by the requirements for the calculation of accurate anterior and posterior corneal power, astigmatism and aberrometry from an *in-vivo* scanning measurement [7]. The difficulty of point scanning approaches is apparent when we consider that an axial error of only 1 μm in a measurement of a corneal radius over a 2.5 mm chord results in an error of about 0.1 Dioptres for a typical eye. Patient eye motion over the acquisition time of a typical OCT scan can be two orders of magnitude higher than this.

The availability of high resolution 2D image sensors, with good sensitivity in the near infrared range, coupled with novel micro-optics technology have made possible the development of 3D snapshot OCT approaches to overcome scanning and subject movement challenges. An early example [8], used a precision milled multifaceted reflective element to map 3D information on to a 2D sensor to demonstrate volume imaging with a limited depth range of 0.4 mm and lateral coverage of less than 3 mm. In this work we have developed an alternative 3D snapshot approach

specifically designed for AS imaging. In particular, we demonstrate how a sparse 2D grid of A-scans covering an area of 16.8×9.6 mm can be registered and resampled into a highresolution 3D volume from which anterior surfaces, including the lens, can be segmented. The small scan angles and sparse 3D sampling are key enablers of accurate anterior and posterior corneal power measurements. Sample images of 3D AS volumes are shown for keratoconus and cataract subjects, the latter with associated maps of anterior and posterior axial curvature, pachymetry, epithelial thickness and axial length retinal profile. With a change of detachable objective lens, we demonstrate high resolution 3D anterior volumes and 3D posterior volumes, the latter being critical for preoperative posterior assessment for cataract surgery.

2. Method

A simplified schematic for anterior mode imaging with the HP-OCT system [9] is shown in Fig. 1(A). The technology shares some of the key components of a spectral-domain OCT (SD-OCT), but adds a 0.4 mm pitch micro-lens array into the sample arm to split the 840 nm superluminescent diode (SLD) light source, with 25 nm bandwidth (providing an axial resolution in air of $12.5 \mu\text{m}$), into 1008 individual beams (henceforth referred to as beamlets) which are imaged onto the eye as a 42×24 grid (with a 0.4 mm pitch) to cover an area of 16.8×9.6 mm. The beamlets have a measured full width half maximum (FWHM) spot size in the focal plane of $29 \mu\text{m}$ and corresponding Rayleigh length of 2.4 mm. A second micro-lens array of the same size and pitch as the imaging array is used in the spectrometer. It has a reduced focal length to increase the numerical aperture of the focused beamlets enabling spot sizes comparable with the pixel size of the sensor whilst maintaining spacing between beamlets.

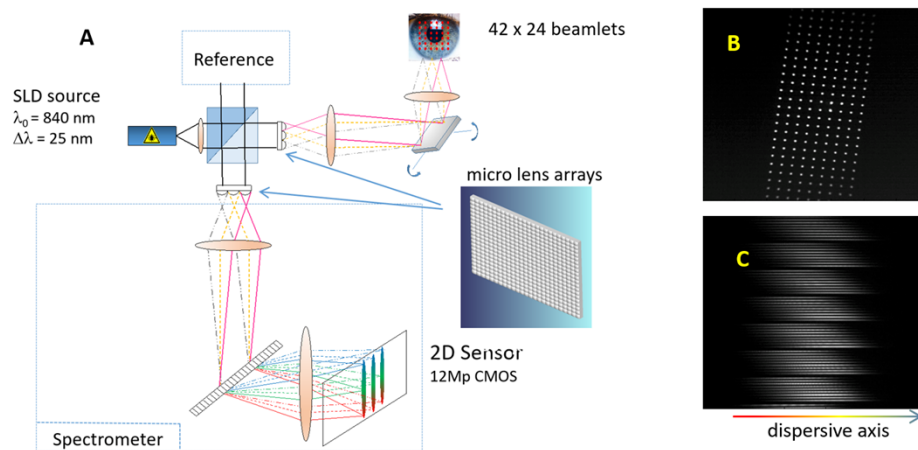


Fig. 1. (A) Simplified schematic of the HP-OCT optical relay. (B) tilted array of beamlets on sensor without dispersion (reduced array size for clarity), (C) dispersed beamlets on sensor.

The collimated beamlets overlap on the grating with a beam diameter of 20 mm and the angle of incidence is determined by the beamlet grid position. The dispersed beams are focused onto a 2D 12 Mpixel monochromatic CMOS sensor array (4096×3072 pixels) with a pixel size of $5.5 \mu\text{m}$. The beamlet exposure time is $100 \mu\text{s}$ at a frame rate of 300 Hz. A small tilt ($< 1/24$ rad) between the axis of the lenslet array and the dispersive sensor axis ensures separation on the sensor of all 1008 spectra which are spread over 3072 rows of the sensor with guard bands between spectra to minimize crosstalk. For illustration, an image of a tilted beamlet array on the sensor without dispersion, using a reduced array size for clarity, is shown in Fig. 1(B). The associated dispersed grid is shown in Fig. 1(C). The pixel resolution in the dispersive axis

(4096 pixels) is 0.016 nm/pixel giving a Nyquist range of 11.2 mm in air. The measured roll-off, decoupled from defocus, is 9 dB at 6 mm depth in air.

Figure 2(A) shows partially processed data obtained from a single snapshot frame, showing how the sparsely sampled volume is captured over the grid of 1008 beamlets as ordered on the sensor. Figure 2(B) shows a 3D view of the frame data where the A-scans are rearranged onto a grid of 0.4 mm pitch. Each frame consists of a grid of $42 \times 24 = 1008$ A-scans and frames are acquired at 300 Hz providing an A-scan rate of 302.4 kHz. The location on the eye of the sparsely sampled volume which is captured in a single frame is scanned over a small range of 0.4 mm to fill in the gaps between points on the grid and create a contiguous dense volume image of the eye as shown in Fig. 2(C). The scanning is much simplified compared to the traditional two axis mechanical scanners as both axes can be scanned simultaneously using a mirror which is precisely placed to ensure distortion-free projection and beamlet shifting over the whole eye. For standard corneal mode imaging 256 frames are captured, in less than 1s. A scan pattern covers a uniform grid of 16 horizontal and 16 vertical scan positions with 25 μm spacing giving a sampling density of 1600 A-scans/mm².

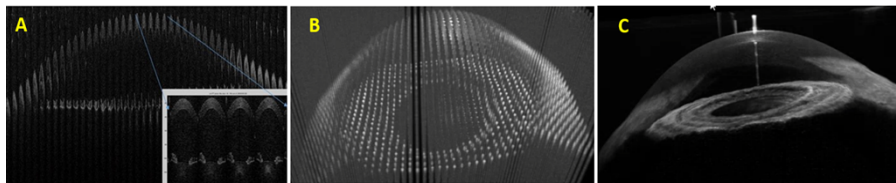


Fig. 2. (A) A single processed frame of the camera showing how the 3D ocular structure is captured in 1008 A-scans. (B) 3D view of processed frame with sparse A-scans rearranged onto 0.4 mm grid. (C) A scan pattern of only 0.4 mm range is used to fill in gaps between A-scans. The final dense corneal volume with voxels of axial and lateral dimensions of 5.4 μm and 37.5 μm respectively is created from combining data from 256 registered frames. A maximum intensity projection of the volume is shown.

A rigid body volume-based registration procedure is used to align frames with a reference volume created from a single up-sampled frame with masking to remove the iris. Registered frames are resampled into a volume with voxels of axial and lateral dimensions of 5.4 μm and 37.5 μm respectively. A Gaussian weighting scheme that is function of distance between the registered A-scans to volume voxel allocates the contribution of A-scans into the resampled volume. Unless specifically prefixed as sparse, the term ‘volume’, will denote a dense resampled volume with voxel sizes of axial and lateral dimensions of 5.4 μm and 37.5 μm respectively. The lateral size was chosen as a practical compromise between resolution, speckle averaging and uniformity. The latter refers to the issue in which patient movement is such that no A-scans fall within a given lateral voxel position.

Although the HP-OCT A-scan rate is very high, the acquisition is parallelised so that this does not impact the dwell time for acquiring data at each point, which is instead limited only by the phase stability requirements of OCT. Importantly, the use of commercially available image sensors together with the parallel read out from the sensors reduces the need for very high-speed serial acquisition of data and highly specialised laser sources which increase both the complexity and cost of OCT systems, particularly for higher A-scan speeds. The mean sensitivity over all beamlets as measured with a mirror at the focal plane (set at 1.5 mm in air from 0 delay) is 106 dB with 1007 beamlets over 95 dB as illustrated in Fig. 3(A).

For both anterior and retinal imaging the exposure levels are compliant with the retinal thermal limits as specified in the IEC 60825-1, ANSI Z136.1 and ISO 15004-2 laser safety standards. In the case of anterior mode imaging, an emmetropic eye sees a diffraction pattern consisting of a grid of ~ 100 spots with a Gaussian envelope of 0.45 mm diameter ($1/e^2$) with corresponding

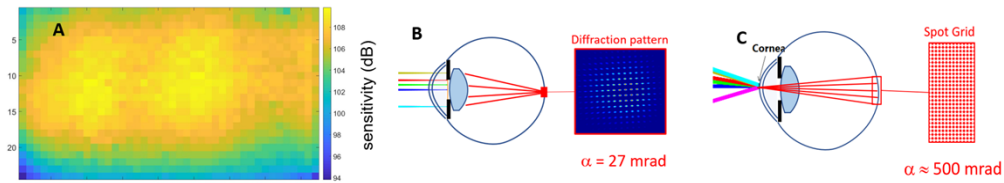


Fig. 3. (A) Sensitivity of 42×24 grid of beamlets. Mean sensitivity is 106 dB with 1007 beamlets over 95 dB. (B) For anterior mode imaging a diffraction pattern generated by the micro-lens array has an angular subtense of 27 mrad (0.45 mm extent on retina) (C) For retinal imaging, each frame images a full grid of 1008 beamlets with minimum angular subtense of 500 mrad.

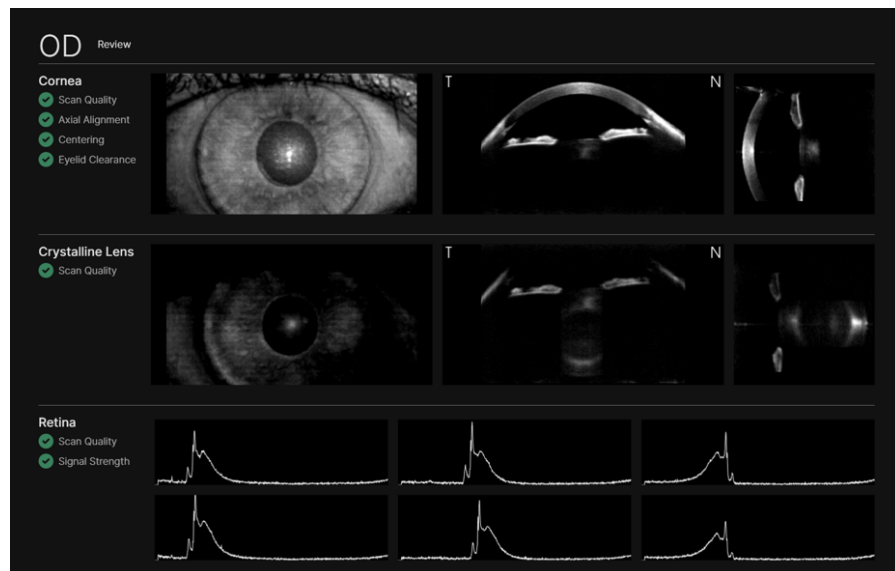


Fig. 4. Image quality metrics captured prior to registration and analysis. The preview volume is quickly generated by aligning frames according to scan pattern only. The first row shows *en-face* and horizontal and vertical slices of the preview volume used for eyelid coverage and alignment metrics. The second and third rows provide scan quality metrics for the lens and axial length measurements respectively.

angular subtense of $\alpha=27 \text{ mrad}$ as illustrated in Fig. 3(B). These spots are not related to individual beamlets, but they are the diffraction orders of the lenslet array. Measurements at the retinal plane of a model eye show that the spot with maximum power contains 0.7% of the total power on the retina. As this diffraction pattern is not a standard retinal irradiance distribution considered by laser safety standards, we followed the conservative approach outlined in IEC 60825-1 section 4.3d for the assessment of non-uniform, non-circular or multiple apparent sources. When considering both single spots as well as every possible sub-aperture comprising multiple spots, the most restrictive evaluation results in a safe accessible emission which is 47% of the class 1 limit. For the case of retinal imaging, we followed the same approach in assessing the retinal irradiance pattern consisting of the regular grid of 42×24 spots covering an area of $9.2 \times 5.2 \text{ mm}$ (minimum angular subtense of $\alpha=500 \text{ mrad}$) as illustrated in Fig. 3(C), and here the most restrictive evaluation also yields a class 1 classification with the accessible emission being only 4% of the class 1 limit.

The capture of 3D frames enables image quality to be estimated rapidly from preview volumes prior to frame registration and full analysis. Figure 4 shows slices extracted from a preview volume in which frames are aligned according to scan position only. Whilst the preview volume does not account for patient movement it enables rapid estimates (< 3 s) of quality measures such as eyelid coverage, subject alignment, scan quality and axial length signal strength. The scan quality metric includes the number of frames with poor SNR caused by phase wash-out from excessive axial movement. To improve the robustness of axial length measurement 6 axial length scans are captured sequentially at 6 axial instrument positions. Preview images of these scans are shown at the bottom row of Fig. 4.

3. Results

3.1. Anterior volume imaging and 3D biometry

Several views through an acquired volume of a subject with keratoconus and an IOL implant are shown in Fig. 5. (The IOL being difficult to see in this volume). The first row shows a maximum projection view of the 3D volume and a horizontal volume slice. The second row shows a vertical volume slice and an *en-face* slice through the cornea. The excellent registration of each of the frames into the volume, demonstrated by the clean anterior and posterior surface edges. The distortion of the cornea due to keratoconus can be visualized in the *en-face* slice showing deviations from the circular interfaces of a normal eye. Volume slices of a cataract subject are shown in Fig. 6. The quality of the registration is manifest in the contrast of epithelium layer which is visible across the whole volume (Fig. 6(B)). Prior to evaluating the epithelium thickness map the contrast of the epithelium layer is further enhanced by 2D directional filtering parallel to surface, the resulting epithelial map over a 4.5 mm radius is shown in Fig. 6(C). For AS capture, inclusive of lens and axial length measurements, a total of 572 frames at 300 Hz are captured.

Figure 7(B) shows anterior and posterior corneal curvature maps and a pachymetry map acquired from topography data of the respective segmented interfaces. Total corneal power maps as well as epithelial maps are also derived from the topographic maps of the corneal surfaces.

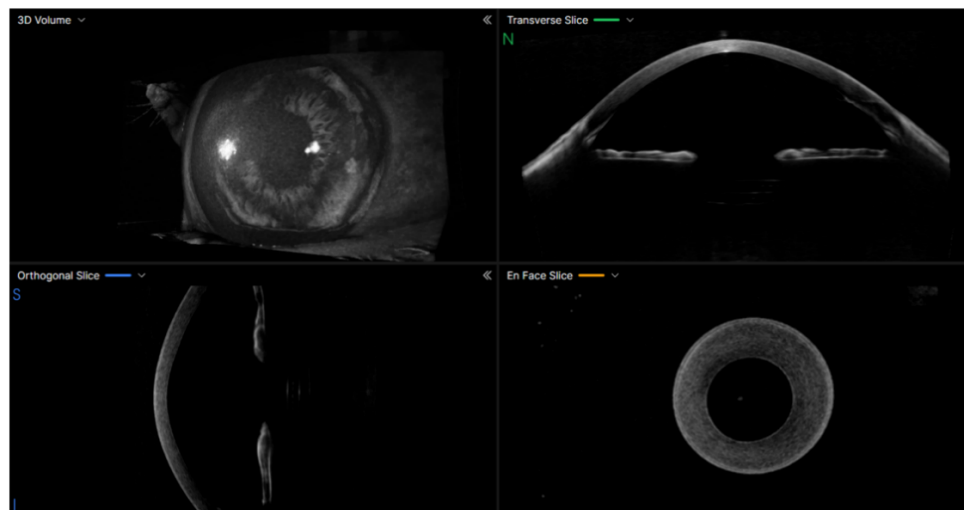


Fig. 5. Various views of the volume data set acquired from a patient with Keratoconus and an IOL implant. The first row shows a 3D maximum projection of the volume data and a horizontal volume slice. The second row shows vertical and *en-face* slices respectively. Keratoconus is apparent in the distortion of the *en-face* slice.

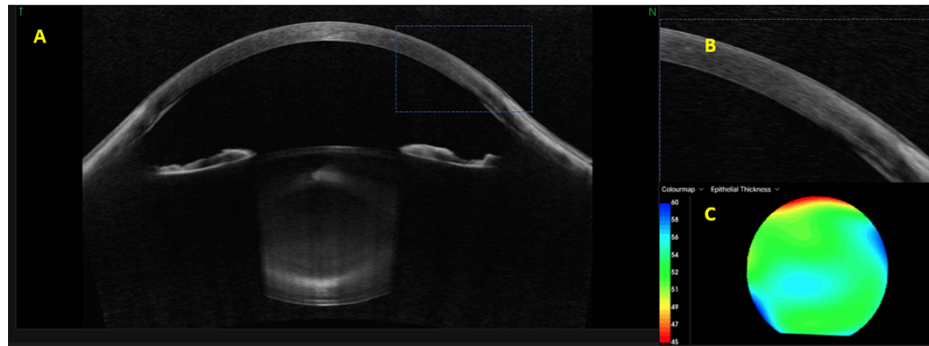


Fig. 6. (A), (B) Anterior volume slice of cataract subject. (C) Epithelial thickness map over 4.5 mm radius.

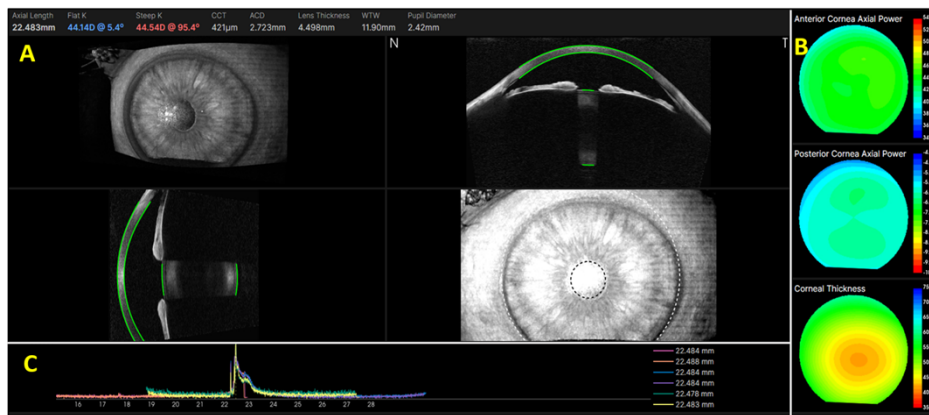


Fig. 7. (A) Biometry measurements derived from an HP-OCT volume data set with volume-based segmentation of cornea and lens surfaces. (B) The anterior and posterior axial curvature and corneal thickness maps cover 9 mm diameter. (C) Axial length measurements from foveal A-scans obtained at 6 different instrument positions

Accurate axial length (AL) assessment is important in monitoring myopia development and interventions and is also a key parameter in cataract and other refractive surgical interventions. Figure 7(C) also shows the simultaneous imaging of the anterior segment and measurement of the axial length. As noted previously, 6 axial length measurements are made at different axial instrument positions. In contrast to the preview images, the profiles are aligned with respect to the corneal apex. Measurement of axial length referenced to the anterior corneal topography eliminates potential measurement errors due to misalignment of the instrument axis with respect to the corneal apex. The large number of beamlets traversing the lens allows multiple paths for the retinal signal in both directions providing the strong cumulative retinal profile. Additionally, the angle of the eye relative to the instrument can be measured (similarly to the lens tilt measurement) so that off-axis measurements of the axial length can be reliably obtained.

3.2. OCT-angiography (OCT-A) and high-resolution anterior imaging

Examples of *en-face* OCT-A in the AS have been relatively uncommon even in the literature, probably due to the difficulties of registration of volumes with enough accuracy. Some studies however have highlighted the capability to image the iris or sclera [4,10,11]. In Fig. 8 we show an early example of an OCT-A *en-face* projection captured over a large area of the AS using

HP-OCT. OCT-A data is obtained by capturing 4 sequential frames (at 300 Hz) at each scan position. An OCT-A volume generated from 4×256 frames is captured in 3.4 s. At each scan position the 4 A-Scans are axially registered and flow determined from intensity-based decorrelation. Angiogram frames are registered using 3D volumetric registration of associated OCT intensity frames and then resampled into a final 3D angiogram.

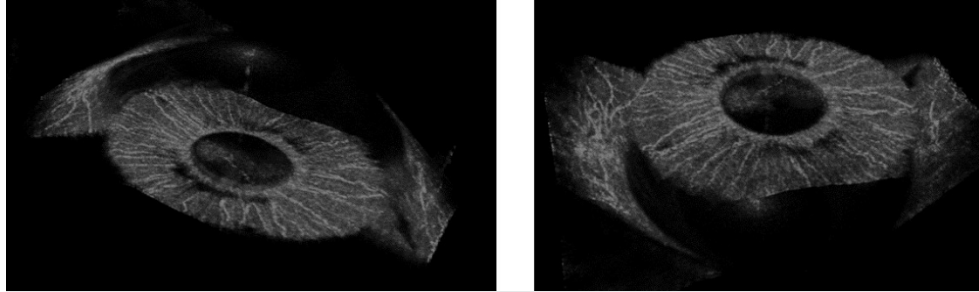


Fig. 8. OCT-A volumes of the sclera and iris presented as 3D maximum projections. The projection can be viewed from in front of the cornea (left) or behind the iris (right) providing excellent visualisation of the vascular structure of the AS.

It is important to note that for HP-OCT, the conventional trade-offs between resolution imaging field and the depth of focus still apply. The use of a shorter wavelength (840 nm) of NIR is advantageous, allowing for approximately 50% deeper depth of focus for a given lateral resolution compared to 1300 nm wavelength. However, enhancing the resolution by reducing the spot size by a factor of 3, results in a reduction of the depth of focus by a factor of 9. Figure 9 shows the enhanced visibility of features in apost-LASIK scarred subject using an interchangeable high-resolution lens to reduce the spot size to $10 \mu\text{m}$.

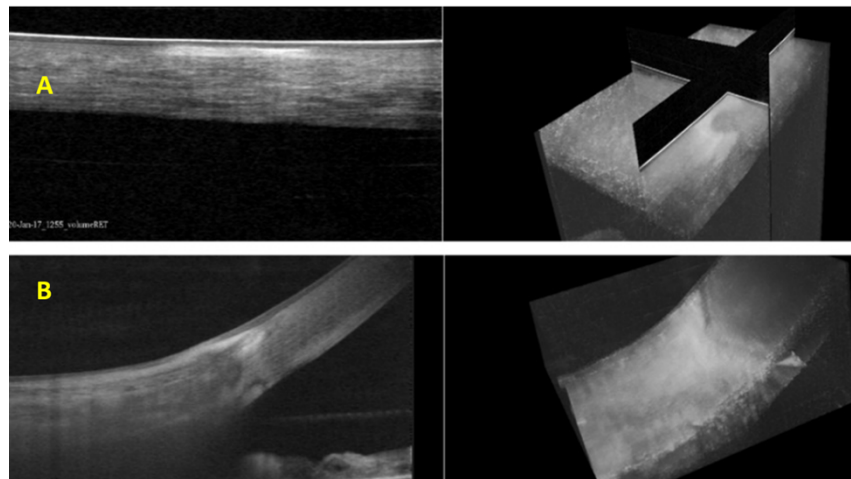


Fig. 9. Images acquired with $10 \mu\text{m}$ lateral resolution by using a detachable high resolution objective lens (A) top left is a horizontal slice created from the 3D volume (top right) showing post-surgical scar tissue on a cornea (B) bottom left is a horizontal slice including sclera derived from the volume image (bottom right).

3.3. Retinal imaging with HP-OCT

The retinal imaging capability of HP-OCT is illustrated in Fig. 10 with examples of retinal volumes (9.2×5.2 mm area) for a normal eye and for a subject with toxoplasmosis. The lateral resolution in the focal plane is $16 \mu\text{m}$. In this patient no eye tracking was used and the patient could not fixate due to the macular damage, yet a high-quality 3D retinal volume was able to be acquired within 512 frames in less than two seconds. A volume slice, showing a typical level of contrast, segmentation result and a RNFL-RPE (Retinal Nerve Fiber Layer to Retinal Pigment Epithelium) thickness map are shown in Fig. 11. We further note a large Nyquist depth range of 8.3 mm (in tissue) and clear choroidal-scleral boundary.

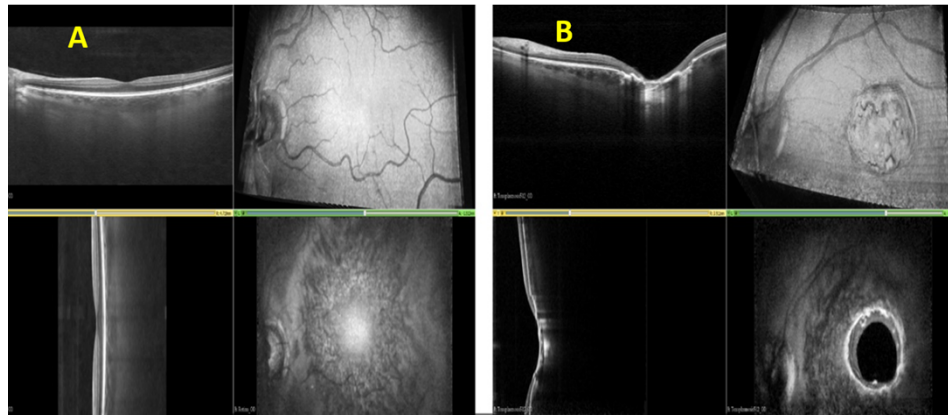


Fig. 10. Volume slicing of retinal images from (A) normal retina and (B) patient with toxoplasmosis. In each case the top right is a volume projection, and the two left images are orthogonal volume slices with the bottom right being an axial slice. Even for the case of the patient without fixation capacity a high-quality retinal volume is obtained allowing easy identification of pathology.

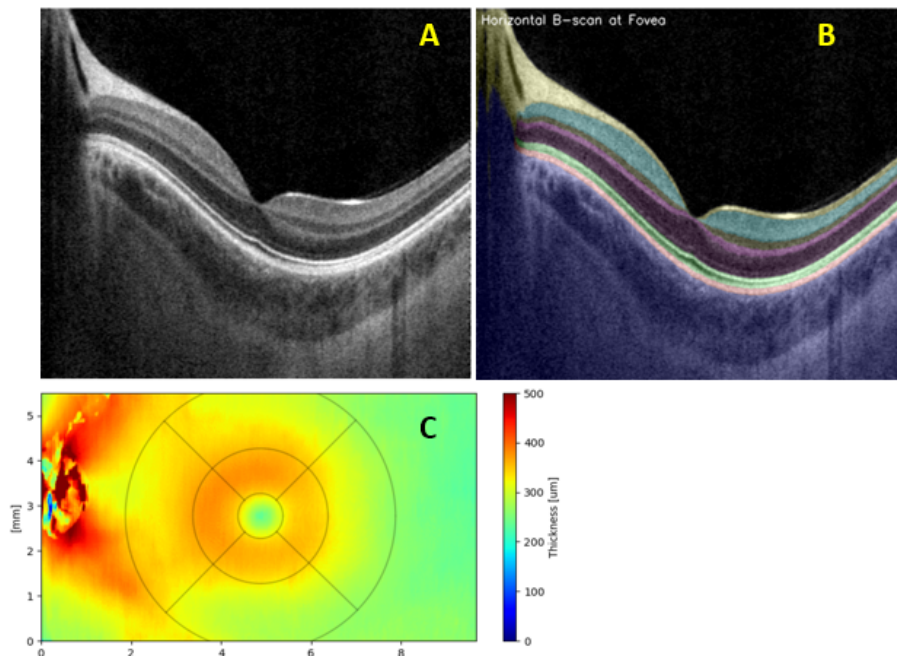


Fig. 11. (A) Horizontal volume slice (B) Eight-layer segmentation (C) RNFL-RPE thickness map.

4. Discussion

In summary, the ability of the HP-OCT 3D snap-shot technique to freeze patient motion over a large field of view is crucial to its ability to ensure accurate biometry. Volumetric registration of 3D frames enables subject movement to be tracked and compensated for over time scales that are ultimately limited only by laser safety standards. Retinal volumes for example, can be captured in 256, 512 or 1024 frame modes. One of the key practical challenges, specific to parallel sampling, includes minimising crosstalk between beamlets by ensuring appropriate guard bands.

In a single instrument, with rapid acquisition, we can acquire all the measurements required for intraocular lens (IOL) calculation formulae. The measurement of posterior corneal power for example, which is completely registered with respect to the anterior corneal surface, means that the total corneal power and astigmatism can be calculated accurately using numerical ray tracing techniques. Furthermore, the full biometry of the eye from the central corneal thickness and pachymetry to the anterior chamber depth and lens tilt, are derived from a volume that is obtained from a single 572 frame acquisition. This can be contrasted with conventional AS-OCT, that provides only orthogonal or radial slices (B-scans) at discrete intervals when imaging the AS. The lens tilt and estimated total lens volume will be valuable tools in predicting the actual IOL position post-surgery providing more accurate estimation of the refractive outcomes. When assessing a patient for suitability for cataract surgery, the same instrument can be used (with an interchangeable objective lens) to acquire retinal volumes to assess the posterior pole health across from the fovea to the optic nerve.

A key clinical application of the HP-OCT is in the specification and assessment of scleral lenses. With an extended scan mode, the HP-OCT will be able to acquire accurate corneal topography out to a diameter of more than 16 mm enabling simulated lens fitting and evaluation of on-eye lens fit over the entire scleral lens. Although this is preliminary research with OCT-A, it is clear that the intensity-based result (4 repeats) provides significantly enhanced detail regarding the

microvascular which could be affected by systemic diseases such as Diabetes, infection, allergy and dry eye [11]. We emphasize that the registration of frames does not require any form of active eye tracking [12], instead we solely rely on volumetric registration of the captured 3D frames to provide images free from motion artefacts. The anterior and posterior modes provide a strong platform for whole-of-eye imaging, with a potential application exploiting the ability to measure both the anterior and posterior segments of the eye with the same instrument enabling an accurate determination of the true retinal shape [13]. Finally, we note that HP-OCT technology offers many future opportunities in both ultra-high resolution imaging [14], wide field imaging and elastography.

5. Conclusion

We have demonstrated highly parallelized spectral domain OCT imaging of the anterior and posterior segments with sparse 2D grids of 1008 A-scans at a frame rate of 300 Hz giving an A-scan rate of 302.4 kHz. The grid of beamlets is generated by placing a 0.4 mm pitch micro-lens array into the sample arm to split an 840 nm SLD light source, with 25 nm bandwidth into individual beams. The dispersed beams are focused onto a 2D 12 Mpixel monochromatic CMOS sensor array. The key benefits of sparse 3D sampling are that it is robust to patient movement and only small scan angles are required to create a dense volume. We demonstrate that software based volumetric registration of sparse 3D frames offers high quality anterior volume imaging and full biometry (using 572 frames) without motion artefacts. The benefit of software-based frame registration is further demonstrated with artefact free examples of AS OCT-A. In addition, we show that with the same platform, we can capture high resolution anterior volumes and importantly, posterior volume images for preoperative assessment of the posterior segment.

Disclosures. SF: Cylite Pty. Ltd. (I, E, P), TA: Cylite Pty. Ltd. (I, E, P), GF: Cylite Pty. Ltd. (I, E, P), DL: Cylite Pty. Ltd. (I, E, P), AS: Cylite Pty. Ltd. (I, E, P).

HP-OCT and Hyperparallel OCT are trademarks of Cylite in some jurisdictions.

Data availability. Data underlying the results presented in this paper are not publicly available at this time but may be obtained from the authors upon reasonable request.

References

1. J. S. Asam, M. Polzer, A. Tafreshi, N. Hirschall, and O. Findl, "Anterior segment OCT," in *High Resolution Imaging in Microscopy and Ophthalmology* (Springer International Publishing, 2019), pp. 285–299.
2. S. B. Wang, E. E. Cornish, J. R. Grigg, and P. J. McCluskey, "Anterior segment optical coherence tomography and its clinical applications," *Clin. Exp. Optom.* **102**(3), 195–207 (2019).
3. D. P. Piñero, "Technologies for anatomical and geometric characterization of the corneal structure and anterior segment: A review," *Semin Ophthalmol* **30**(3), 161–170 (2015).
4. W. Di. Lee, K. Devarajan, J. Chua, L. Schmetterer, J. S. Mehta, and M. Ang, "Optical coherence tomography angiography for the anterior segment," *Eye and Vision* **6**(1), 4 (2019).
5. D. Hammer, R. Daniel Ferguson, J. Magill, M. White, A. Elsner, and R. Webb, "Image stabilization for scanning laser ophthalmoscopy," *Opt. Express* **10**(26), 1542–1549 (2002).
6. A. Unterhuber, B. Považay, A. Müller, O. B. Jensen, M. Dülk, T. Le, P. M. Petersen, C. Velez, M. Esmateelpour, P. E. Andersen, and W. Drexler, "Simultaneous dual wavelength eye-tracked ultrahigh resolution retinal and choroidal optical coherence tomography," *Opt. Lett.* **38**(21), 4312–4315 (2013).
7. E. Kim and K. Ehrmann, "Assessment of accuracy and repeatability of anterior segment optical coherence tomography and reproducibility of measurements using a customised software program," *Clin. Exp. Optom.* **95**(4), 432–441 (2012).
8. T. Nguyen, M. C. Pierce, L. Higgins, and T. S. Tkaczyk, "Snapshot 3D optical coherence tomography system using image mapping spectrometry," *Opt. Express* **21**(11), 13758–13772 (2013).
9. T. Anderson, T. A. Segref, G. Frisken, and S. Frisken, "3D spectral imaging system for anterior chamber metrology," *Proc. SPIE* **9312**, 93120N (2015).
10. A. S. Kang, R. J. Welch, K. Sioufi, E. A. T. Say, J. A. Shields, and C. L. Shields, "Optical coherence tomography angiography of iris microhemangiomas," *Am J Ophthalmol Case Rep* **6**, 24–26 (2017).
11. T. Akagi, A. Uji, A. S. Huang, R. N. Weinreb, T. Yamada, M. Miyata, T. Kameda, H. O. Ikeda, and A. Tsujikawa, "Conjunctival and intrascleral vasculatures assessed using anterior segment optical coherence tomography angiography in normal eyes," *Am. J. Ophthalmol.* **196**, 1–9 (2018).

12. P. Zang, G. Liu, M. Zhang, C. Dongye, J. Wang, A. D. Pechauer, T. S. Hwang, D. J. Wilson, D. Huang, D. Li, and Y. Jia, "Automated motion correction using parallel-strip registration for wide-field en face OCT angiogram," *Biomed. Opt. Express* **7**(7), 2823 (2016).
13. R. P. McNabb, J. Polans, B. Keller, M. Jackson-Atogi, C. L. James, R. R. Vann, J. A. Izatt, and A. N. Kuo, "Wide-field whole eye OCT system with demonstration of quantitative retinal curvature estimation," *Biomed. Opt. Express* **10**(1), 338 (2019).
14. T. Anderson, A. Segref, A. G. Frisken, H. Ferra, D. Lorensen, and S. Frisken, "3D Spectral domain computation imaging," *Proc. SPIE* **9697**, 96970Z (2016).